ADVANCED ENGINEERING MATERIALS
www.aem-journal.com

Toughness of Confined Auxetic Foams

*Adrianos E. F. Athanasiadis, Oliver Duncan, Michal K. Budzik, and Marcelo A. Dias**

Auxetic (negative Poisson's ratio) materials offer benefits such as impact mitigation, thermal insulation, vibration damping, and reduced deviatoric/shear strain—a key measure of material failure risk. However, the fracture mechanics of auxetic materials remain largely unexplored. This study investigates damage initiation and propagation in confined re-entrant foam structures exhibiting auxetic behavior. These structures are fabricated by thermo-mechanical transformation of pristine polyurethane foams. The confined foam is especially relevant for mechanical joints and bonding, illustrating practical advantages. Experimental mechanical characterization, combined with Ogden's hyperelastic formulation, underpins the analysis of the confined foam within a fracture mechanics framework, further supported by a traction-separation law. A one-dimensional semi-analytical model, integrating beam theory and experimental material properties, predicts fracture processes under a double cantilever beam configuration. The model shows a very good agreement with experimental results, with confidence intervals ranging from 67% to 83%. The fracture toughness of the auxetic foams is reliably quantified, revealing the influence of the microstructural conversion process and a 50% improvement over conventional foams. This work transforms conventional foams by leveraging auxetic behavior for superior mechanical performance and provides a comprehensive investigation into their fracture mechanisms, offering critical insights for designing next-generation mechanical joints and bonding technology.

1. Introduction

Auxetic materials contract (or expand) in the direction perpendicular to an applied compressive (or tensile) load, thereby exhibiting a somewhat counterintuitive negative Poisson's ratio. In mechanical metamaterials such as auxetic foam, this negative Poisson's ratio emerges as a larger-scale structural response, after careful manipulations of the small-scale constituents.[1] Auxetic foams were first made during the late 1980s[2,3] and have since been widely fabricated and tested.[4–9] Often considered within the broader class of mechanical metamaterials and lattice materials,[10] auxetic materials open exciting possibilities in various fields. Namely, applications of auxetics include impact protection, sports equipment, medical devices, aerospace, and construction.[9,11,12] Across these sectors, auxetic materials are transforming the way we approach design, damage mitigation, and overall performance.

Here we focus on unique mechanical properties of auxetic materials, namely their ability to maximize volumetric strain and minimize deviatoric (shear) strain.[4] This function can potentially reduce the concentration of stress at the tips of propagating cracks, thereby decreasing the likelihood of material failure. Deviatoric strain is known to enhance stress concentrations that drive crack propagation.[13] Given these conceptual advantages of auxetic materials, it is noteworthy that the detailed characterization of crack tip propagation in auxetic foams has not been extensively studied.

The tendency of auxetic foams to undergo volumetric rather than deviatoric deformation makes them ideal for applications requiring high resilience and durability under extreme loads. Beyond mechanical performance, auxetic materials have also been explored as proof-of-concept platforms for adhesive bonding scenarios,[14] where recent studies suggest that thick and architected bondlines offer distinct advantages.[15–17] Specifically, these engineered bondlines facilitate improved stress distribution within sandwich cores over extended regions compared to conventional adhesives,[15] holding promise for transformative applications in aerofoil and wind turbine blade design.[18,19] These developments build on a growing understanding of cellular solid fracture and failure mechanisms,[20] including the formation of metamaterial failure maps. Notably, certain confined architected materials exhibit enhanced toughness when subjected to loads exceeding crack onset, demonstrating a potential for mitigating fracture propagation.[16]

A. E. F. Athanasiadis, M. A. Dias
Institute for Infrastructure and Environment
School of Engineering
The University of Edinburgh
Edinburgh EH9 3FG, UK
E-mail: marcelo.dias@ed.ac.uk

O. Duncan
Department of Engineering
Manchester Metropolitan University
Manchester M1 5GD, UK

M. K. Budzik
Department of Mechanical and Production Engineering
Aarhus University
Aarhus N 8200, Denmark

The ORCID identification number(s) for the author(s) of this article can be found under https://doi.org/10.1002/adem.202500626.

DOI: 10.1002/adem.202500626

Despite these promising advancements, current confined architected systems tend to exhibit stiffness-driven failure, undergoing either brittle or elastoplastic fracture. This behavior is largely dictated by their most used fabrication method, additive manufacturing, which imposes constraints on material properties and structural integrity. Additionally, the scalability of architected bondlines remains a challenge due to size limitations and extended production times.[21,22] These constraints not only hinder widespread adoption but also complicate fracture characterization, as reliable crack growth measurements necessitate long and uniform samples.[23,24] Consequently, the full potential of architected bondlines in enhancing structural toughness and longevity has yet to be fully realized.

In this study, we use auxetic foams to demonstrate how the bulk volume of thick adhesive bondline systems can be substituted,[15,16,25,26] to overcome the limitations of established, and current state-of-the-art, manufacturing techniques. Auxetic foams are manufactured using the established thermomechanical process, capable of producing large, anisotropic samples, that are relatively homogenous at the mesoscale, following **Figure 1**.[27–31] The foams are then characterized under the Ogden hyperelastic material model[32] (Figure 1b) that serves as a basis to formulate a custom nonlinear cohesive zone law.[33–35] Thereafter, we fabricate double cantilever beam (DCB) specimens by bonding the produced foam to acrylic beams that we test in mode I fracture loading (Figure 1d). The DCB configuration is a standardized testing setup for inducing mode I fracture loads in confined systems. The main advantage of the DCB configuration is the ability to control the length of the fracture process zone[15,17] through the dimensions of the system. The shape and length of the process zone for linear elastic materials have been studied extensively, and the existing analytical models for the DCB configuration can yield very accurate results regarding the stress distribution close to the crack tips, that are proportional to the beams local deflection. However, such models are limited to small strains and displacements and linear materials. We develop a custom 1-dimensional numerical model utilizing a Euler–Bernoulli beam on elastic foundation (Winkler) assumptions[36,37] for comparing our experimental results (Figure 1c). A very good agreement with the experimental results is displayed.

The accuracy of our model allows us to estimate the strain energy release rate during the damage propagation. Hence, we use a framework from fracture of composite materials and delamination to calculate the critical strain energy release rate for the converted foams, namely expressing the strain energy release rate as a function of the crack length[38,39] (Figure 1e). We show, on an Ashby plot, that these auxetic foams are superior to currently available materials.[40] The biaxial tensile state, caused by the negative Poisson ratio of the foam and evidenced by digital image correlation, restricted the development of the propagating crack.

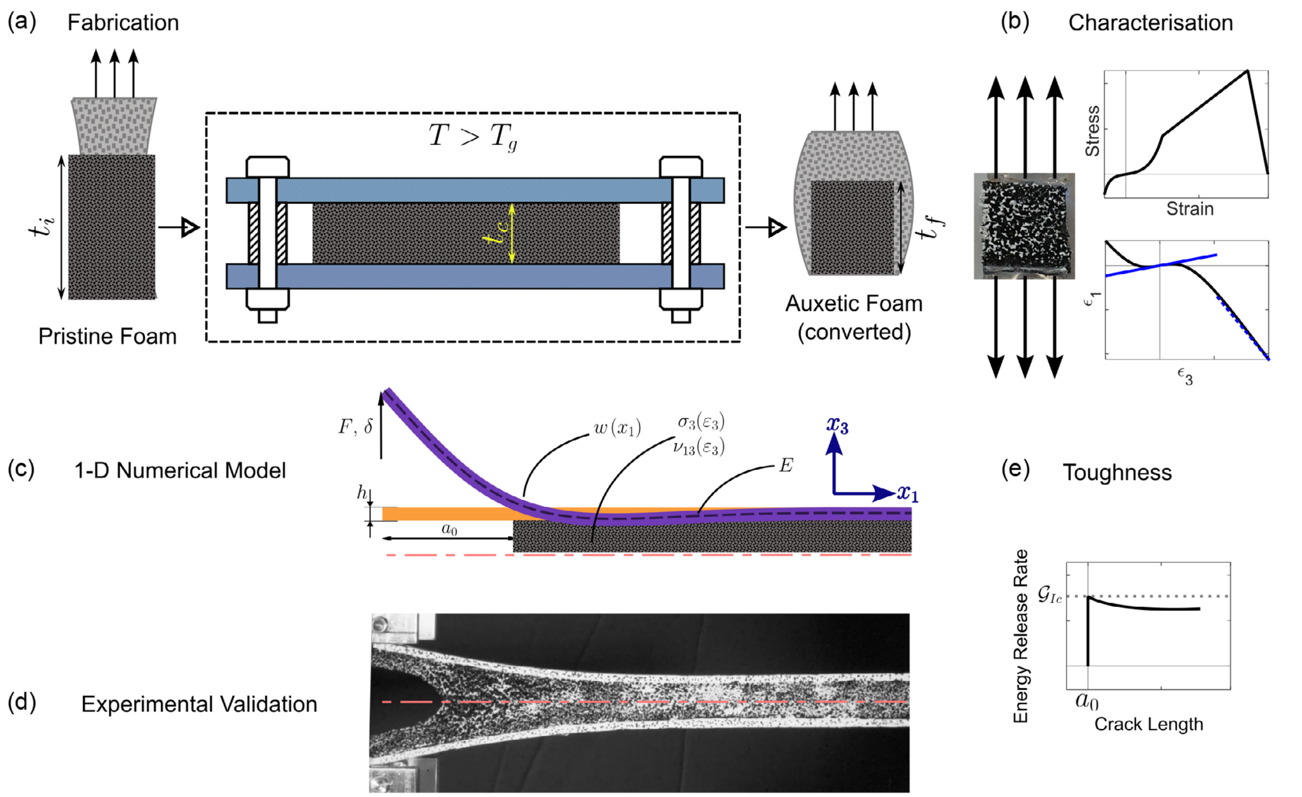

Figure 1. Schematic diagram illustrating the sequential steps undertaken in this study: a) the foam conversion framework; b) material characterization via uniaxial tensile testing; c) application of a one-dimensional double cantilever beam (DCB) model to simulate decohesion; d) estimation of the foam's fracture toughness; and e) validation of the model through Mode I fracture experiments.

2. Constitutive Modeling of Foams and Damage Law

2.1. Material Model

To accurately capture mechanics of the auxetic foams, we employ the Ogden hyperelastic model, which is well suited for materials undergoing large deformations. This model allows us to describe the highly nonlinear stress–strain response of auxetic foams and provides robust analytical tools to then later describe their damage phenomenology. By integrating this model within the context of fracture mechanics and complementing it with a decohesion model, we aim to develop a comprehensive understanding of the material's performance in mechanical joints and bonding scenarios.

All produced foams display a hyperelastic response, and the methodology implemented here is adapted from Ciambella et al.[32] This approach is based on the assumptions that dissipative effects during quasi-static deformations are negligible, and that the macroscopic response of the foam is not overly affected by transverse/biaxial deformation, due to the small Poisson's ratio (as is also the case for similar foam in ref. [32]). A relationship between the transverse strain to the loading direction, ε_1, and the strain in the direction of the load, ε_3, is defined as follows

$$\varepsilon_1(\varepsilon_3) = -\frac{\nu_a \varepsilon_3}{(1+\pi\nu_a^2\varepsilon_3^2)^q} - \nu_b\varepsilon_3 \tag{1}$$

where $q = 1/2 + (\pi\nu_a\varepsilon_I)^{-2}/2$ is an exponent that relates to the transition zone between two asymptotic extremes. The strain ε_I is defining the transition point, and ν_a and ν_b are fitting parameters defining the bounds for the material's Poisson's ratio, which vary with applied deformation. Therefore, Equation (1) gives rise to the Poisson's ratio in the $(3,1)$-direction (with the first index denoting the loading direction and the second index denoting the transverse direction)

$$\nu_{31}(\varepsilon_3) := -\frac{\varepsilon_1}{\varepsilon_3} = \frac{\nu_a}{(1+\pi^2\nu_a^2\varepsilon_3^2)^q} + \nu_b \tag{2}$$

Specifically, two limits are presented: i) when $\varepsilon_3 \to 0$, then the apparent Poisson's ratio of the material is $\nu_{31} \to \nu_a + \nu_b$; ii) whereas when $\varepsilon_3 \gg \varepsilon_I$, then the apparent Poisson's ratio of the material is $\nu_{31} \to \nu_b$. Furthermore, the stress–strain relationship for the material model reads as follows

$$\sigma_3(\varepsilon_3) = \sum_{i=1}^{n} \frac{\mu_i}{1+\varepsilon_3}\left[(1+\varepsilon_3)^{\alpha_i} - (1+\varepsilon_1(\varepsilon_3))^{\alpha_i}\right] \tag{3}$$

where μ_i and α_i are fitting parameters related to the shear modulus of the system. In this study, we choose $n = 2$, $\mu_1 > 0$, and $\mu_2 < 0$, which means that $\alpha_1 > 0$ and $\alpha_2 < 0$. These choices satisfy the constraint $\mu_i\alpha_i > 0$. The effective shear modulus of the system can be estimated as $2\mu = \sum_n \mu_i\alpha_i$.

The fitting material parameters are chosen through a two-objective least square optimization scheme. By defining the two absolute errors for stress–strain response and Poisson's ratio, as in

$$\phi_i = |\sigma_3^i - \hat{\sigma}_3^i|, \quad \text{and} \quad \psi_i = |\varepsilon_1^i - \hat{\varepsilon}_1^i| \tag{4}$$

with the quantities under the *hat* referring to the experimental values. Therefore, the objective function is given by

$$\mathcal{F} = (\mu_i, \alpha_i, \nu_i, \varepsilon_I) = \sum_j \phi_j^2 + \sum_j \psi_j^2 \tag{5}$$

where the sum is performed over the experimental data points. The problem is subject to the following constraints: $\mu_i\alpha_i > 0$, $-1 \leq \nu_a < 0 < \nu_b < 1/2$, and $\varepsilon_I + 1 > 0$. These are set through the bounds of the parameters.

2.2. Decohesion Model

The DCB test is a widely used method for evaluating the fracture toughness of materials, particularly in bonded joints and composite structures. By applying the DCB setup to auxetic foams, we can gain insights into their unique deformation characteristics and crack propagation mechanisms. To accurately model the decohesion process, we employ the Euler–Bernoulli beam theory on a nonlinear elastic foundation. This approach allows us to capture the complex interactions between the beam and the auxetic foam core, providing a comprehensive framework for analysing the material's response under loading conditions. In the following, we detail the mathematical formulation and how we extract the numerical solution of the decohesion model, which is crucial for predicting the performance of auxetic foams in applications.

Therefore, let us begin by stating the Euler–Bernoulli beam theory on a nonlinear elastic foundation:[17,36]

$$B\frac{\mathrm{d}^4 w(x_1)}{\mathrm{d}x_1^4} + H(x_1 - a)\sigma(\varepsilon_3) = 0 \tag{6}$$

where $B \approx Eh^3/12$ is the bending rigidity (with E as the beam's Young's modulus and h its thickness), $w(x_1)$ is the deflection function, $H(x-a)$ is the Heaviside step function, and a is the initial crack length. Here, the nonlinearity stems from Ogden's hyperelastic constitutive model of the foundation, following Equation (3), and we provide their representation in both plane stress and plane strain forms, respectively, as follows

$$\sigma(\varepsilon_3) = \begin{cases} \dfrac{\sigma_3(\varepsilon_3)}{1-\nu_{31}^2(\varepsilon_3)}, & \text{for plane stress} \\[2ex] \dfrac{\sigma_3(\varepsilon_3)[1-\nu_{31}(\varepsilon_3)]}{[1+\nu_{31}(\varepsilon_3)][1-2\nu_{31}(\varepsilon_3)]}, & \text{for plane strain} \end{cases} \tag{7}$$

where the reaction stress applied from the core material to the beam. The strain $\varepsilon_3(w) = 2w(x_1)/c$ is the local strain of the core material expressed through the deflection function, and c is the thickness of the core. Due to the nonlinearity of the stress function, the boundary value problem of eq:bvp1 is solved numerically with the following decomposition into a first-order system of four equations as

$$\frac{\mathrm{d}}{\mathrm{d}x_1}\begin{bmatrix} w(x_1) \\ \varphi(x_1) \\ M(x_1) \\ Q(x_1) \end{bmatrix} = \begin{bmatrix} \varphi(x_1) \\ 12(Eh^3)^{-1}M(x_1) \\ Q(x_1) \\ -H(x_1-a)\sigma(\varepsilon_3) \end{bmatrix} \tag{8}$$

where $\varphi(x_1)$, $M(x_1)$, and $Q(x_1)$ are the rotation, moment, and shear force functions of the beam, respectively. The system of eq:bvp_sys is solved with the bvp5c function in MATLAB. The boundary conditions at $x_1 = 0$ are $w(0) = \delta$ and $M(0) = 0$ to ensure displacement controlled and moment-free conditions at the loaded end of the beam. At the other end of the beam, $x_1 = a + L_c$, we assume moment and shear force are zero. Hence, we demand $M(a + L_c) = 0$ and $Q(a + L_c) = 0$, where L_c is the length of the bonded part of the beam. The reaction force at the loaded end is retrieved by evaluating the shear force at that point, i.e., $F = Q(0)$.

3. Results and Discussion

3.1. Material Characterization

The converted foams are characterized and modelled according to Ogden's hyperelastic model, which has been formulated in sec:Ogden. Transverse and longitudinal strain measurements are performed using digital image correlation (DIC) in order to formulate a Poisson's ratio function relationship (**Figure 2**a). The calculated shear modulus of the pristine foam is significantly higher than that of the converted foams, while an increase in the conversion temperature results to higher shear moduli as

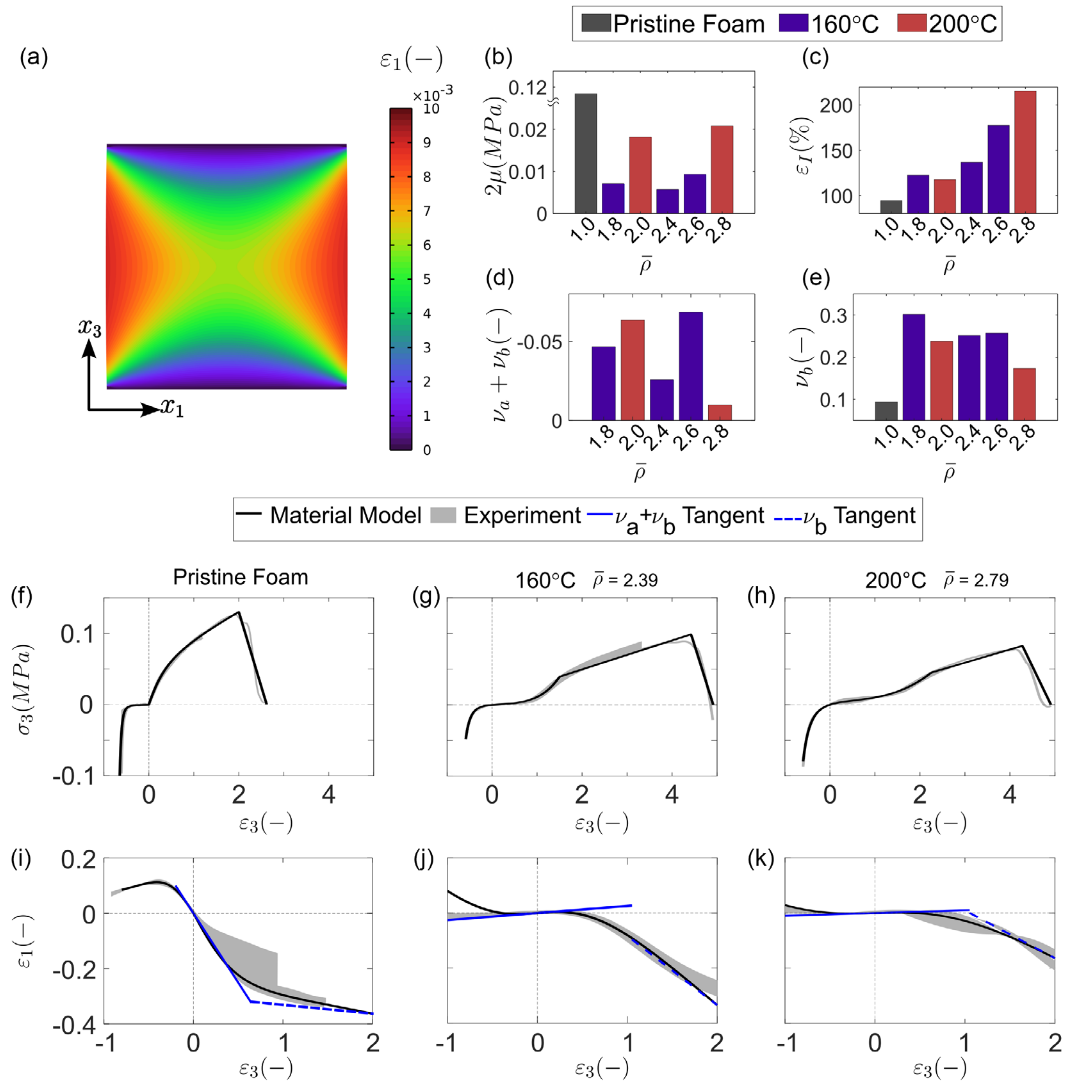

Figure 2. Measured foam material properties. a) Transverse strain ε_1 contours of a specimen, representing what is obtained via digital image correlation (DIC). b) Measured shear modulus, showing that converted foams have an order of magnitude lower tensile shear modulus compared to the pristine foam. c) Transitional strain measure ε_I, which indicates that denser foams (with lower conversion ratios) maintain their auxetic behavior over larger strains. d) Effective Poisson's ratio at small strains, where all converted foams exhibit moderate auxetic behavior. e) Effective Poisson's ratio at large strains, showing that converted foams display a significantly higher Poisson's ratio than the pristine foam under high strain values. f–h) Stress–strain curves for representative foam types, with both experimental data and the corresponding adapted material models. i–k) Transverse–longitudinal strain curves for the same foam types. Here, panels (f,i) correspond to the pristine foam; panels (g,j) to foam converted at 160 °C for linear compression ratios $LCR_3 = 33\%$ (yielding a relative density $\bar{\rho} = 2.39$); and panels (h,k) to foam converted at 200 °C for $LCR_3 = 33\%$ (yielding $\bar{\rho} = 2.79$). The y-axis scales are identical across panels (f–h) and (i–k).

displayed in Figure 2b. All converted foams have auxetic behavior in the low longitudinal strain regimes (<50%) Figure 2d.

Since the foams were compressed only in the x_3 direction during conversion, they exhibit auxetic behavior specifically in the directions corresponding to Poisson's ratios ν_{31} and ν_{32}. Under small deformations, the stiffness of uniaxially compressed auxetic foams in x_3 is much lower than x_1 or x_2, which remains similar to that of the unconverted foam.[28] As such, according to the symmetric compliance condition ($E_3\nu_{13} = E_1\nu_{31}$), Poisson's ratio ν_{31} and ν_{32} are relatively low.[13] When loaded past the transitional strain value (ε_I), measured as per Figure 2c, samples are no longer auxetic and exhibit positive (true) Poisson's ratios between 0.2 and 0.3 (Figure 2e). In Figure 2f–h, the stress–strain response of selected specimens is presented. The proposed semi-analytical model accurately captures the mechanics in the reversible regimes, with the elastic limit identified as the point where tensile force reduction occurs due to local yielding. Furthermore, we assume that the behavior past the recoverable regime follows a linear hardening profile accounting for plasticity, and a steeper linear softening regime when damage occurs. That completes the list of elements needed to implement a Cohesive Zone Model (CZM).[33–35]

In Figure 2i–k, the relationship between transverse (ε_1) and longitudinal strain (ε_3) is presented for the same sample. Their mechanical behavior is also well captured during the reversible regimes. Beyond the yield point, we assume a constant Poisson's ratio that is given by the value of ν_b. Taking the Normalized Root Mean Square Error (NRMSE) between the Ogden model predictions and the experimental data, $1 - \text{NRMSE}$, gives confidence bounds of 88% for the stress-strain data and 82% for the axial vs transverse strain data. Hence, this semi-analytical model can form a basis for evaluating damage phenomena when such materials are used in confined systems.

3.2. Fracture Toughness

In this section, we experimentally examine the DCB configurations and fracture toughness of the materials. Once again, strains and beam deflections were measured using DIC and then compared to the results of the semi-analytical model (**Figure 3**a–c). In Figure 3d–f, the load response curve for pristine foam is shown, where experimental data are compared to results of the model. The load response curves for pristine and selected converted foams demonstrate the accuracy of the proposed one-dimensional model (Figure 3d–f). A very good agreement is observed between the experimental results and the one-dimensional model, with NRMSE between predicted and measured curves yielding confidence intervals between 67% and

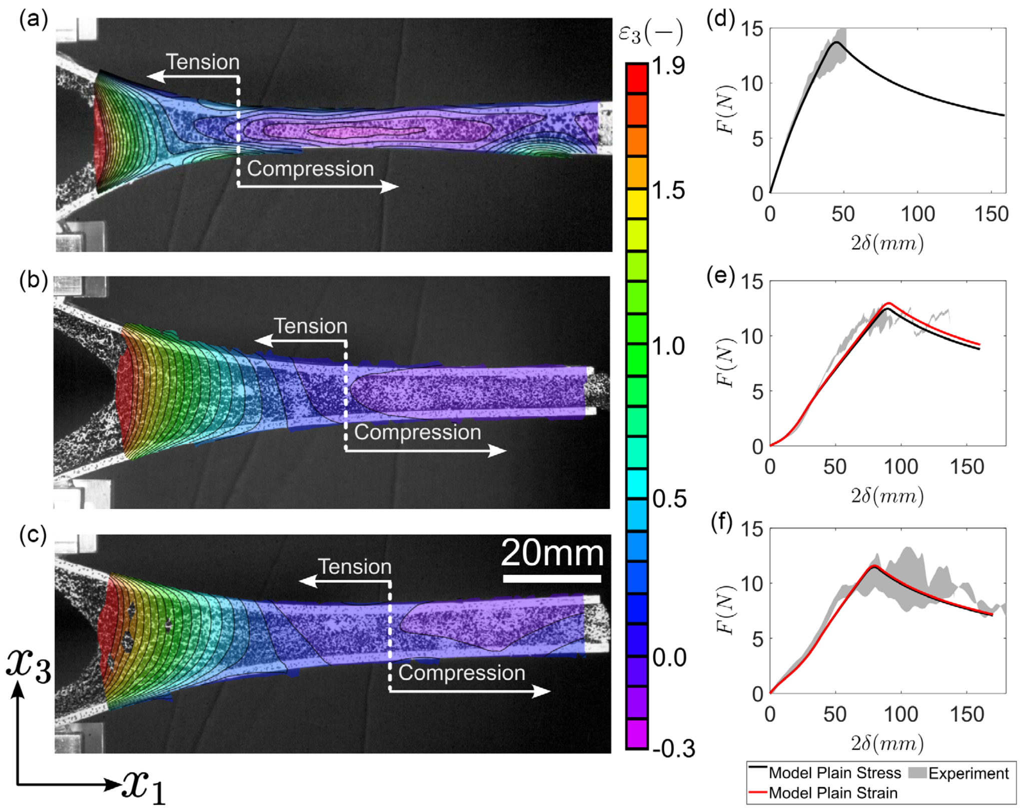

Figure 3. Double cantilever beam (DCB) experiments designed to evaluate decohesion and damage propagation in foam materials. a–c) Specimen geometry and normal strain distribution measured at the core during loading, captured using digital image correlation (DIC). d–f) Load–response curves comparing experimental data with predictions from the semi-analytical decohesion and damage propagation model. Panels (a,d) pertain to the pristine foam; panels (b,e) to foam converted at 160 °C for $\text{LCR}_3 = 33\%$ (yielding $\bar{\rho} = 2.39$); and panels (c,f) to foam converted at 200 °C for $\text{LCR}_3 = 33\%$ (yielding $\bar{\rho} = 2.79$).

83%, regardless of the choice of plane stress or plane strain. Moreover, the model displays exceptional accuracy before crack onset and efficiently captures the change of slope corresponding to the fracture process zone transitioning from the response displayed in Ogden model to a linear damage type hardening.

The strain energy release rate in mode I loading (G_I) of the auxetic foam can be calculated by recalling[38,39]

$$G_I = \frac{Eh^3}{8 \times 3^{1/3}} \left(w|_{x_1=0}\right)^{2/3} \left(\left.\frac{\mathrm{d}^3 w}{\mathrm{d}x_1^3}\right|_{x_1=0}\right)^{4/3} \tag{9}$$

where E, h, and $w(x_1)$ are, respectively, the Young's modulus, thickness, and deflection curve of the adherent. In this context, the deflection curve must be of at least C^3 continuity. The critical value of the strain energy release rate is calculated as the maximum value of G_I **Figure 4** and is generally higher than other foams, including other auxetic foams from ref. [41]. Herein, we observe a stark toughening of the material during the conversion process at 160 °C. However, the foams converted at 200 °C were less tough than the pristine foams. Similar PU foams have been frequently shown, through thermogravimetric analysis, differential scanning calorimetry, and infrared spectroscopy, to degrade at 200 °C.[9,42–45] Following similar thermomechanical conversions, this degradation also coincides with the increase in foam stiffness and reduction in observed magnitude of Poisson's ratio, which is observed in Figure 2. Therefore, it is likely that the reduction in toughness under the higher conversion temperatures is caused by similar degradation of the intrinsic polymer, making these trends consistent with previous work. As such, auxetic foams provide new design capabilities, by simultaneously increasing toughness while maintaining a low density.

4. Conclusions

This study has demonstrated the superior toughness of auxetic foams compared to their conventional counterparts, highlighting their potential use in challenging applications. The strain energy release rate, calculated as a function of crack length, enabled the

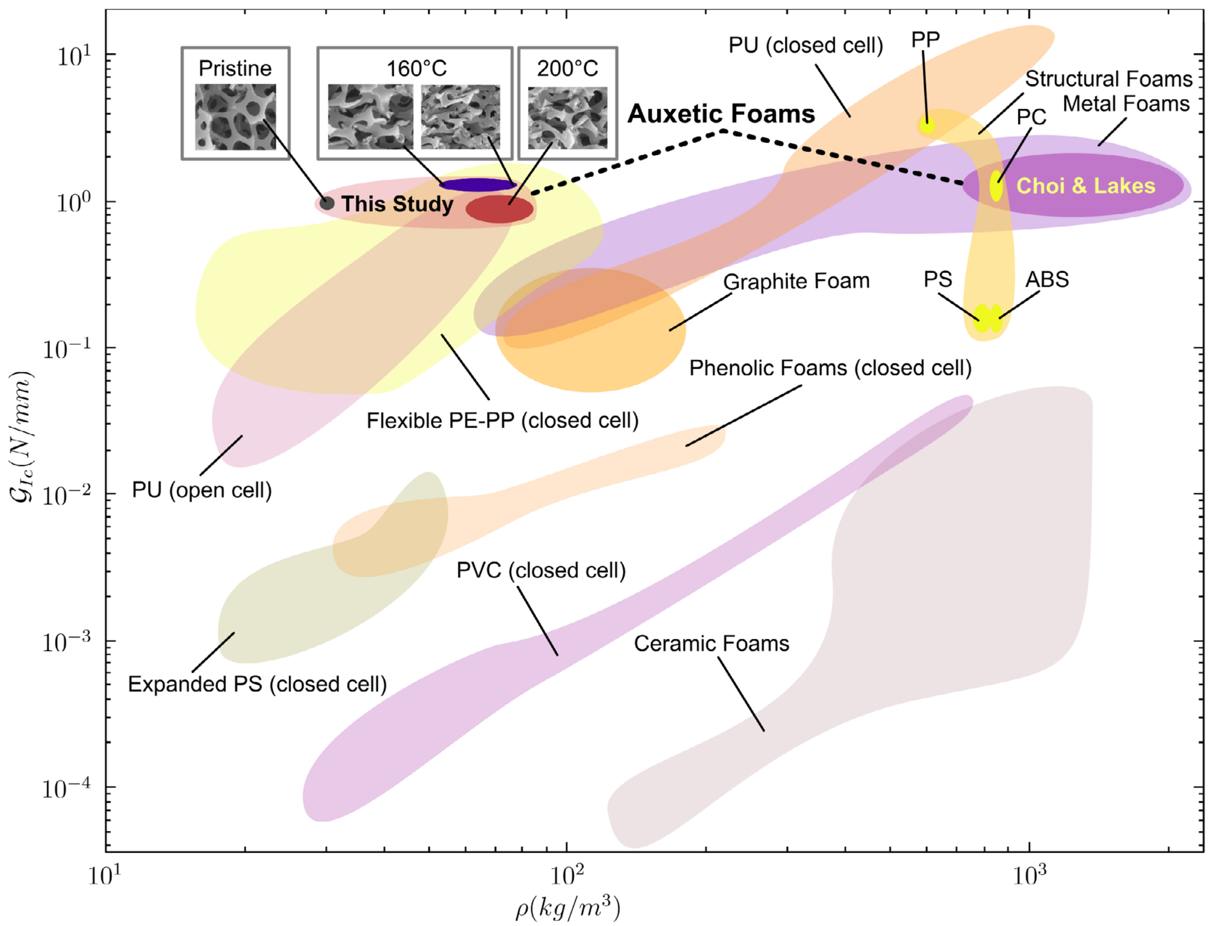

Figure 4. Ashby-type chart comparing the critical strain energy release rate, G_{Ic}, in Mode I, for various foam types. The data were extracted from the fracture toughness K_{Ic} and converted to G_{Ic} using the relation $G_{Ic} = K_{Ic}^2/E$. The chart displays results from the present study (1.24–1.43 N mm^{-1} for foams converted at 160 °C and 0.72–1.10 N mm^{-1} for foams converted at 200 °C) along with literature values from ref. [41] (1.4–2.1 N mm^{-1}), which represent the only available data of this kind to the authors' knowledge. The stock (pristine) foam exhibited a toughness of 1.00 N mm^{-1} in this study (compared to 0.8 N mm^{-1} in ref. [41]). Notably, conversion to an auxetic structure leads to an increase in toughness, surpassing the range typical of open-cell polyurethane foams. Chart adapted from Granta Selector.r2.[46]

determination of the fracture toughness of the foams, showing an increase of up to 50% over conventional foams.

Our investigation made use of the Ogden hyperelastic model to define a nonlinear traction-separation law, which successfully captured the mechanical behavior of the foams. This semi-analytical model, integrated into a one-dimensional numerical framework using Euler–Bernoulli beam theory and a nonlinear elastic foundation, accurately simulates the mode I fracture phenomenology in the DCB configuration. The model's predictions of load responses and deflection curves during both loading and fracture showed excellent agreement with experimental data, validating its performance before crack onset and during crack initiation. This reliability ensures the model's applicability for practical uses and further studies.

Additionally, we provided a detailed experimental methodology of foam behavior during fracture loading, which is critical for material design. Our accurate representation of the complex mechanics of auxetic foams enables precise design of materials for specific applications.

In summary, auxetic foams showed up to 50% higher strain energy release rates than conventional foams. These new findings offer new insights into the fracture mechanics of auxetic materials and pave the way for their optimized design in structural applications. We also present a computationally efficient semi-analytical model, which is robust for estimating mode I fracture toughness of nonlinear confined systems, benchmarked against the auxetic and conventional foams. This novel framework paves the way for future advancements in material design and fracture analysis across a range of applications, from biomedical devices to impact-resistant structures. The modeling approach simplifies the analysis of complex fracture mechanics, making it computationally efficient while retaining accuracy.

5. Experimental Section

Foam Conversion: During the conversion process, the foam is heated above glass transition temperature in a prestressed state, to cause through-thickness micro-buckling. When cooled back to room temperature, the foams lock in their buckled, re-entrant cellular structure. The converted foams are then measured and inspected using scanning electron microscopy to establish an understanding of the small scale morphology of the converted foams compared to the pristine foam.

Pristine 30 PPI reticulated poly-urethane foam was supplied by RGH Rubber and plastics. The density of the pristine foam was 30 kg m^{-3}, and the foam cell rise was in the x_3 direction. The initial dimensions of each foam block were $150 \times 150 \times 32$ mm (x_1, x_2, x_3). Each piece of foam was placed between two 5 mm aluminium sheets, then compressed in the x_3 direction with linear compression ratios of 50%, 33%, and 25%, respectively. Thereafter, each set was heated at 160 and 200 °C in a Carbolite PF60 oven for 30 min, then left to cool (while maintaining compression) in the open oven overnight. Finally, each set of converted foam was left stress free for 24 h, to recover nonresidual deformation, with final dimensions recorded to determine the foam density. Based on the thickness recovery, we can measure the initial compression and final compression ratios. Subsequently, the final density of the converted foam is estimated. Post conversion, the foam was observed in a HITACHI TM4000Plus Scanning Electron Microscope at 50× and 150× magnification in order to qualitatively characterize the effects of conversion.

Converted Foam Morphology: Measurements suggest that converted foams heated to 160 °C exhibit significant thickness recovery (ranging from 7% to 14%) once the supporting frame is removed, as expected.[42] For foams heated at 200 °C, however, the observed recovery was less than measurement error.

Scanning electron microscopy was applied to foam sections, which were cut using a pristine utility knife blade (Stanley), without any applied coating. The pristine foam **Figure 5**b exhibits uniform cells with a slight cell rise in the x_3 direction while being orthotropic in the x_1, x_2 plane. The cell span is of the order of 0.63 mm for pristine foam, while in the case of converted auxetic foams, the cell span is smaller, with little change in the x_1 and x_2 directions, while shrinking by 40–59% in x_3, following the

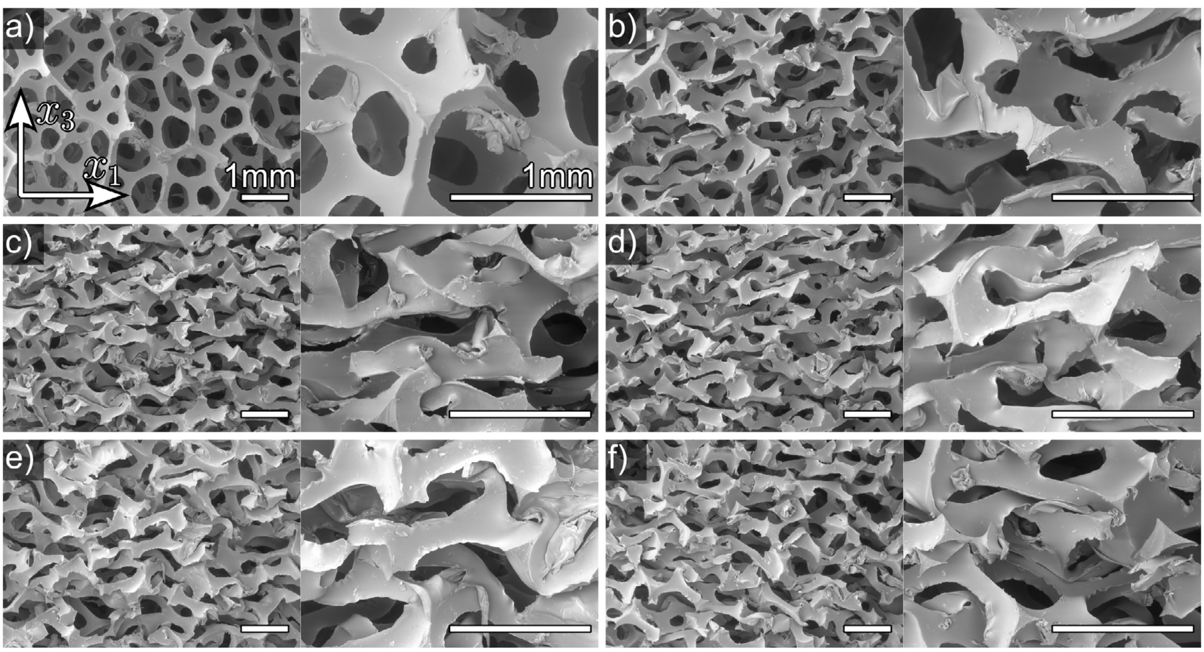

Figure 5. Morphology of the produced foams, as revealed by scanning electron microscopy (SEM). Images are presented at 50× and 150× magnifications. a) Pristine foam. b–d) Foams converted at 160 °C with LCR$_3$ of 50, 33, and 25%, respectively. e,f) Foams converted at 200 °C for LCR$_3$ values of 50% and 33%, respectively. All images share a common coordinate system and include a scale bar representing 1 mm.

Table 1. Foam Properties measurements.

T [°C]	LCR_3 [%]	FCR_3 [%]	ρ [kg m^{-3}]	$\bar{\rho}$ [−]	ℓ_3 [mm]
Pristine	100	100	30.00	1.00	0.63 ± 0.16
160	50	57	52.75	1.76	0.37 ± 0.15
	33	42	71.64	2.39	0.29 ± 0.09
	25	39	77.42	2.58	0.26 ± 0.10
200	50	50	60.00	2.00	0.38 ± 0.13
	33	36	83.84	2.79	0.30 ± 0.10

compression ratios applied. The specific values of linear compression ratios (LCR_3), final compression ratios (FCR_3), density (ρ), relative density ($\bar{\rho} = (30\text{kg/m}^3)^{-1}\rho$), and unit cell length in x_3 (ℓ_3) are displayed in **Table 1**. Due to the conversion conditions, the converted foams are re-entrant only in the x_3 direction and orthotropic in the x_1, x_2 plane as well.[30]

Uniaxial Testing: In DCB testing, the foam specimens' core is bonded between two acrylic beams, as shown in Figure 1; the beam ends were clamped in hinged, moment-free aluminum grips. A mode I opening was imposed by vertically separating the grips in a universal tensile testing machine, while a camera recorded displacements in the sample with a DIC technique (shown in Figure 3). Three approximately 10 mm × 10 mm × 10 mm cubes were cut from each fabricated foam using a fresh utility blade (Stanley) in order to setup uniaxial tension-compression specimens. The cubic samples were then bonded to acrylic end blocks with Araldite 2-part (fast dry) epoxy resin and mounted into the universal tensile machine (Tinius Olsen, H50KS, with a 1 kN load cell). We performed one cycle of cyclic tension-compression experiments for two specimens of each fabricated foam at a deformation rate of 12 mm min^{-1} test speed. The third specimen was tested to failure under tension. The transverse and longitudinal strains were obtained by full-field strain measurement using digital image correlation (VIC2D). Images were obtained with a Phantom Miro, R111 camera and a Nikon, AF Nikkor 24–85 mm lens, with 85 mm optical zoom and resolution set to 1280 × 800 pixels at 24 fps.

Testing of Confined Specimens: To fabricate DCB specimens, three samples of each type of foam were cut using a fresh utility blade (Stanley), into rectangles with dimensions: 150 mm × 10 mm × 10 mm (x_1, x_2, x_3). These were bonded to two acrylic sheets (PMMA) with thickness 2 mm, using 2-part epoxy resin (Araldite, Rapid). The bonding surfaces of the acrylic sheets were treated with grain 80 abrasive paper and cleaned with 74% methylated spirit. A thin film of adhesive was applied, to avoid adhesion of cell ribs within the bulk of the sample. A mass of 500 g was used to support the system while curing. Lastly, rectangular end blocks with cylindrical holes were bonded as above, and a pre-crack was cut with the utility blade.

To test the confined DCB configurations, we mount the specimen into the universal testing machine using aluminum pinned grips. In that way we are able to apply a vertical force and vertical displacement with minimal friction and without inducing rotation. Three DCB tests were undertaken on separate samples of each type of foam, at 60 mm min^{-1} and with a preload between 0.24 and 0.5 N. Image acquisition for use with DIC was performed with the same equipment as for the uniaxial tests. The laboratory temperature and humidity conditions were 20–25 °C and 40–60%, respectively.

Supporting Information

Supporting Information is available from the Wiley Online Library or from the author.

Acknowledgements

M.A.D. thanks UKRI for support under the EPSRC Open Fellowship scheme (Project No. EP/W019450/1).

Conflict of Interest

The authors declare no conflict of interest.

Author Contributions

Adrianos E. F. Athanasiadis: formal analysis (lead); investigation (lead); validation (lead); visualization (lead); writing—original draft (lead). **Oliver Duncan**: conceptualization (supporting); investigation (supporting); methodology (supporting); supervision (equal); writing—review & editing (equal). **Michal K. Budzik**: conceptualization (supporting); investigation (supporting); methodology (supporting); supervision (equal); writing—review & editing (equal). **Marcelo A. Dias**: conceptualization (lead); funding acquisition (lead); investigation (supporting); methodology (supporting); project administration (lead); supervision (equal); writing—review & editing (equal).

Data Availability Statement

Data sharing is not applicable to this article as no new data were created or analyzed in this study.

Keywords

auxetic foams, fracture toughness, mechanical metamaterials, negative Poisson's ratio

Received: March 4, 2025
Revised: April 16, 2025
Published online:

[1] R. Lakes, *J. Mater. Sci.* **1991**, *26*, 2287.
[2] R. Lakes, *Science* **1987**, *235*, 1038.
[3] K. E. Evans, *Endeavour* **1991**, *15*, 170.
[4] K. E. Evans, A. Alderson, *Adv. Mater.* **2000**, *12*, 617.
[5] J. N. Grima, R. Gatt, P. Farrugaia, A. Alderson, K. E. Evans, in *Proceedings of the International Mechanical Engineering Congress and Exposition*, ASME, volume Aerospace, Orlando, Florida, USA **2005**, 489.
[6] T.-C. Lim, in *Stress Concentration, Fracture and Damage in Auxetic Materials*, Springer Singapore, Singapore **2015**, pp. 147–169.
[7] R. S. Lakes, *Annu. Rev. Mater. Res.* **2017**, *47*, 63.
[8] X. Ren, R. Das, P. Tran, T. D. Ngo, Y. M. Xie, *Smart Mater. Struct.* **2018**, *27*, 023001.
[9] W. Jiang, X. Ren, S. L. Wang, X. G. Zhang, X. Y. Zhang, C. Luo, Y. M. Xie, F. Scarpa, A. Alderson, K. E. Evans, *Composites Part B: Eng.* **2022**, *235*, 109733.
[10] M. Ashby, *Philos. Trans. R. Soc. A: Math. Phys. Eng. Sci.* **2006**, *364*, 1838.
[11] H. M. A. Kolk, A. A. Zadpoor, *RSC Adv.* **2017**, *7*, 5111.
[12] O. Duncan, T. Shepherd, C. Moroney, L. Foster, P. D. Venkatraman, K. Winwood, T. Allen, A. Alderson, *Appl. Sci.* **2018**, *8*, 6.
[13] S. P. Timoshenko, J. N. Goodier, in *Theory of Elasticity*, 3 ed., McGraw-Hill, New York **1970**.

[14] C. P. Puspaningtyas, A. Jusuf, B. K. Hadi, A. Yudhanto, *Heliyon* **2024**, *10*, e24141.
[15] A. E. Athanasiadis, M. A. Dias, M. K. Budzik, *Extreme Mech. Lett.* **2021**, *48*, 101411.
[16] M. L. Hedvard, M. A. Dias, M. K. Budzik, *Int. J. Solids Struct.* **2024**, *288*, 112600.
[17] A. E. Athanasiadis, M. K. Budzik, D. Fernando, M. A. Dias, *Eur. J. Mech. A Solids* **2024**, *105*, 105277.
[18] P. Zuo, A. P. Vassilopoulos, *Int. Mater. Rev.* **2021**, *66*, 313.
[19] B.-H. Xu, J.-H. Guo, A. Bouchaïr, *Int. J. Adhes. Adhes.* **2020**, *98*, 102517.
[20] A. J. D. Shaikeea, H. Cui, M. O'Masta, X. R. Zheng, V. S. Deshpande, *Nat. Mater.* **2022**, *21*, 297.
[21] N. Khan, A. Riccio, *Prog. Aerosp. Sci.* **2024**, *149*, 101021.
[22] N. Rogkas, C. Vakouftsis, V. Spitas, N. D. Lagaros, S. K. Georgantzinos, *Micromachines* **2022**, *13*, 5.
[23] R. Lopes Fernandes, M. K. Budzik, R. Benedictus, S. Teixeira de Freitas, *Compos. Struct.* **2021**, *266*, 113687.
[24] S. T. de Freitas, M. K. Budzik, in *Advances in Structural Adhesive Bonding (Second Edition)* (Ed: D. A. Dillard), Woodhead Publishing in Materials, Woodhead Publishing, Sawston, Cambridge **2023**, pp. 615–641.
[25] S. Mohsenizadeh, R. Alipour, M. Shokri Rad, A. Farokhi Nejad, Z. Ahmad, *Mater. Des.* **2015**, *88*, 258.
[26] G. Z. Fan, X. Ren, S. L. Wang, C. Luo, Y. M. Xie, *Case Stud. Construct. Mater.* **2022**, *17*, e01159.
[27] M. Bianchi, F. Scarpa, M. Banse, C. Smith, *Acta Mater.* **2011**, *59*, 686.
[28] O. Duncan, T. Allen, L. Foster, T. Senior, A. Alderson, *Acta Mater.* **2017**, *126*, 426.
[29] Q. Zhang, W. Lu, F. Scarpa, D. Barton, K. Rankin, Y. Zhu, Z.-Q. Lang, H.-X. Peng, *Mater. Des.* **2021**, *211*, 110139.
[30] Q. Zhang, X. Yu, F. Scarpa, D. Barton, K. Rankin, Z.-Q. Lang, D. Zhang, *Composites, Part B* **2022**, *237*, 109849.
[31] Q. Zhang, X. Yu, Y. Xia, D. Zhang, R. S. Lakes, K. W. Wojciechowski, F. Scarpa, *Composites, Part B* **2024**, *286*, 111791.
[32] J. Ciambella, A. Bezazi, G. Saccomandi, F. Scarpa, *J. Appl. Phys.* **2015**, *117*, 184902.
[33] D. Dugdale, *J. Mech. Phys. Solids* **1960**, *8*, 100.
[34] *Advances in Applied Mechanics* (Eds: G. Barenblatt, H. Dryden, T. von Kármán, G. Kuerti, F. van den Dungen, L. Howarth, Vol. *7*, Elsevier, Amsterdam **1962**, pp. 55–129.
[35] A. Hillerborg, M. Modéer, P.-E. Petersson, *Cem. Concr. Res.* **1976**, *6*, 773.
[36] M. F. Kanninen, *Int. J. Fract.* **1973**, *9*, 83.
[37] D. A. Dillard, B. Mukherjee, P. Karnal, R. C. Batra, J. Frechette, *Soft Matter* **2018**, *14*, 3669.
[38] M. K. Budzik, J. Jumel, M. E. R. Shanahan, *Soft Matter* **2012**, *8*, 8321.
[39] M. K. Budzik, J. Jumel, M. E. R. Shanahan, *J. Adhes.* **2012**, *88*, 885.
[40] M. Ashby, *Acta Metall.* **1989**, *37*, 1273.
[41] J. B. Choi, R. S. Lakes, *Int. J. Fract.* **1996**, *80*, 73.
[42] O. Duncan, F. Clegg, A. Essa, A. M. T. Bell, L. Foster, T. Allen, A. Alderson, *Phys. Status Solidi B* **2019**, *256*, 1800393.
[43] M. Bianchi, F. Scarpa, C. Smith, G. R. Whittell, *J. Mater. Sci.* **2010**, *45*, 341.
[44] K. Boba, M. Bianchi, G. McCombe, R. Gatt, A. C. Griffin, R. M. Richardson, F. Scarpa, I. Hamerton, J. N. Grima, *ACS Appl. Mater. Interfaces* **2016**, *8*, 20319.
[45] R. Critchley, I. Corni, J. A. Wharton, F. C. Walsh, R. J. Wood, K. R. Stokes, *Phys. Status Solidi B* **2013**, *250*, 1963.
[46] ANSYS, Inc., Granta Selector, version R2025. ANSYS, Inc. **2025**, https://www.ansys.com/products/materials/granta-selector, (Accessed: February, 2025).